Image processing for limited aperture inverse acoustic obstacle scattering

D. Russell Luke
PIMS
Simon Fraser University
Burnaby BC V5A 1S6, CANADA

Roland Potthast
Institut for Numerical and Applied Mathematics
University of Göttingen
Germany

Image processing for limited aperture inverse acoustic obstacle scattering.

D. Russell Luke and Roland Potthast [1]

Abstract. This work combines inverse obstacle scattering theory in a limited aperture setting with image processing techniques for synthesizing several independent numerical reconstructions. We employ the *point source method* in a limited aperture setting to locate the boundary of a sound-soft obstacle. The point source method is a numerical algorithm for reconstructing parts of the boundary of an unknown obstacle from partial far-field data generated by one or more incident plane waves. Outside the region of validity for the reconstruction, one encounters systematic errors. These artifacts are well understood and, in some sense, predictable even though the shape and precise location of the obstacle are unknown. We use a priori knowledge about the physics of scattering and about the point source method to synthesize several independent local boundary reconstructions into global boundary reconstructions without artifacts. These techniques include filtered averaging and logical image processing. We illustrate this methodology with examples from simulated data.

Key words. inverse problems, scattering theory, image processing

AMS subject classifications. 35R30, 35P25, 68U10, 94A08

1. Introduction. When we presented this work in seminars and colloquia at the beginning of 2002, a common question from our audiences was in what sense inverse scattering theory, logical image processing, and statistical image processing are connected. Each of these is a field by itself. However, one of the characteristic features of ill-posed inverse problems is that their solutions frequently require a synthesis of ideas from separate, well-delineated disciplines. In other words, necessity is the mother of invention. Medical doctors, for example, routinely synthesize measurements from several different sources to solve the inverse problem of determining why someone is ill. A doctor combines different data sets, a theoretical understanding of the physical processes behind each data set, and a lot of experience to make a logical best estimate. In a similar fashion, we propose logical and statistical image processing techniques that combine different data sets, a theoretical understanding of the mathematical and physical processes behind each data set, and experience to reconstruct an unknown, sound-soft obstacle from several incomplete far-field measurements.

Recent methods for reconstructing the boundary of obstacles from far field data [3, 7, 1] require measurements from a large number of incident waves. In many practical situations such complete information is not possible. In this work we study techniques that use *a single* incident wave. We combine the results from several such reconstructions at several frequencies (less than 10) and directions (at most 4) to obtain a complete estimate of the boundary.

We begin with a review the theory for obstacle reconstruction in a limited aperture setting. In section 2 we investigate the application of the *point source method* proposed by Potthast [9, 10]. In section 3 we discuss image processing strategies used in conjunction with the point source method for obstacle reconstruction. The image processing techniques we study include logical processing, introduced in section 3.1, and filtered weighted averages, reviewed in section 3.2. While these techniques would

---

[1]Institut for Numerical and Applied Mathematics, University of Göttingen, Germany; http://www.scienceatlas.de/nfg

in practice be combined, we study the numerical performance of each separately in section 4 to illustrate the strengths and weaknesses of each.

THE FORWARD MODEL. We consider scattering of small amplitude, monochromatic, time harmonic waves from a sound-soft obstacle embedded in an isotropic homogeneous medium. The obstacle is described by the bounded domain $\Omega \subset \mathbb{R}^m$ ($m = 2$, or 3) with a connected, piecewise C^2 (twice continuously differentiable) boundary $\partial \Omega$ with well behaved corners [5] and the outward unit normal ν. Since the medium is isotropic and the fields are single frequency time harmonic waves, we study fixed frequency scalar waves, $v : \mathbb{R}^m \backslash \overline{\Omega} \to \mathbb{C}$. To avoid notational clutter we suppress any explicit dependence of the field v on the wave number κ. In later sections, however, we consider multiple frequencies and the dependence on κ is included in the argument of the field. Given a continuous function $f : \partial\Omega \to \mathbb{C}$, the field $v \in C^2(\mathbb{R}^m \backslash \overline{\Omega}) \cap C(\mathbb{R}^m \backslash \Omega)$ satisfies the *Helmholtz equation* with *Dirichlet boundary conditions:*

$$(1.1) \qquad\qquad \triangle v(x) + \kappa^2 v(x) = 0, \;\; x \in \mathbb{R}^m \backslash \overline{\Omega},$$

$$(1.2) \qquad\qquad\qquad v(x) = f, \;\; x \in \partial\Omega,$$

where $\triangle$ denotes the Laplacian. Additionally, we impose the *Sommerfeld radiation condition*

$$(1.3) \qquad\qquad r^{\frac{m-1}{2}} \Big(\frac{\partial}{\partial r} - i\kappa \Big) v(x) \to 0, \;\; r = |x| \to \infty.$$

The scattering problem based on the above model is stated as follows:

SCATTERING PROBLEM: *For a sound-soft scatterer Ω and time harmonic waves in a homogeneous medium, given an* incident field $v^i : \mathbb{R}^m \to \mathbb{C}$ *that is an* entire solution *to Eq.(1.1), find the* total field $v : \mathbb{R}^m \backslash \Omega \to \mathbb{C}$ *satisfying Eq.(1.1) on $\mathbb{R}^m \backslash \overline{\Omega}$ with $v = 0$ on $\partial\Omega$ and with $v = v^i + v^s$, where v^s is the* scattered field *satisfying Eq.(1.1) and the Sommerfeld radiation condition Eq.(1.3).*

It is well known, that the scattering problem has a unique solution [4]. The scattered field v^s has the asymptotic behavior

$$(1.4) \qquad v^s(x) \;=\; \frac{e^{i\kappa|x|}}{|x|^{\frac{(m-1)}{2}}} \left\{ v^\infty(\hat{x}) + O\Big(\frac{1}{|x|}\Big) \right\}, \;\; |x| \to \infty,$$

where the function $v^\infty : \mathbb{S} \to \mathbb{C}$ is known as *far field pattern,*

$$\mathbb{S} := \{ x \in \mathbb{R}^m \,|\, |x| = 1 \} \quad \text{and} \quad \hat{x} := \frac{x}{|x|}.$$

Of particular interest is the field resulting from excitation by *plane waves*. We denote this special field by

$$(1.5) \qquad\qquad u = u^s + u^i \quad \text{where} \quad u^i(x) \;:=\; e^{i\kappa x \cdot d}, \;\; x \in \mathbb{R}^m.$$

Here $d \in \mathbb{S}$, denotes the *direction of incidence*. As with the frequency, wherever possible we avoid notational clutter by suppressing the dependence of u^i on d. When necessary we write the dependence explicitly in the argument of the fields as $u(\cdot, d, \kappa)$, $u^s(\cdot, d, \kappa)$, and $u^i(\cdot, d, \kappa)$ respectively.

The point source method described below also makes use of the *dual* to the scattered fields due to incident plane waves, that is scattered fields due to incident *point sources*. Let $\Phi(x, z)$ $(x \neq z)$ denote the free space fundamental solution to the Helmholtz equation at frequency κ in two or three dimensions respectively. We denote the field resulting from excitation by a point source $\Phi(x, z)$ $(x \neq z)$ by $w(\cdot, z) : \mathbb{R}^m \backslash \overline{\Omega} \to \mathbb{C}$:

$$(1.6) \qquad w(\cdot, z) := w^i(\cdot, z) + w^s(\cdot, z), \quad \text{where} \quad w^i(\cdot, z) := \Phi(\cdot, z), \quad z \in \mathbb{R}^m \backslash \overline{\Omega},$$

The field w satisfies Eq.(1.1)-(1.2) for the boundary condition $f = 0$ on $\partial\Omega$. This field is the *Green function* for the boundary value problem Eq.(1.1)-(1.3), and is symmetric:

$$w(x, z) = w(z, x) \quad x, z \in \mathbb{R}^m \backslash \overline{\Omega}, \quad x \neq z.$$

The corresponding scattered field $w^s(\cdot, z)$ satisfies Eq.(1.1)-(1.3) with $f = -\Phi(\cdot, z)$ on $\partial\Omega$.

LIMITED APERTURE SCATTERING. Let $\Lambda \subset \mathbb{S}$ denote an open set of directions on $\mathbb{S}$. We define the *far field operator* restricted to Λ for a far field corresponding to the scatterer Ω, $F_\Omega : L^2(\Lambda) \to L^2(\mathbb{S})$, by

$$(F_\Omega g)(\hat{x}) := \int_\Lambda u^\infty(\hat{x}, -d)g(-d)ds(d), \quad \hat{x} \in \mathbb{S}.$$

The signs in the expression above might seem peculiar, but they are chosen in such a way that the backprojection mapping between the far field measurements and the scattered field which we derive below has a very natural interpretation in terms of a physical aperture in the far field. To hint at this, by the standard far field reciprocity relation [4, Theorem 3.13], the above expression can be written as

$$(F_\Omega g)(\hat{x}) = \int_\Lambda u^\infty(d, -\hat{x})g(-d)ds(d), \quad \hat{x} \in \mathbb{S}.$$

Note that the function g is only defined on $-\Lambda$ where $-\Lambda$ is the rotation of the interval Λ around the unit circle 180 degrees: $d \in \Lambda \iff -d \in -\Lambda$. The far field, however, is defined on Λ with any incident wave direction $-\hat{x}$. In the discussion below it will become clear that the density g is naturally defined on this *virtual* aperture $-\Lambda$ corresponding to the physical aperture Λ on which all of our sensors lie. When $\Lambda = \mathbb{S}$ this virtual aperture is not as apparent.

Similarly, define the operator $H : L^2(\Lambda) \to L^\infty(\mathbb{R}^m)$ by

$$(Hg)(x) := \int_\Lambda e^{i\kappa x \cdot (-d)}g(-d)ds(d), \quad x \in \mathbb{R}^m.$$

We call the function $v(x) = (Hg)(x)$ the *limited aperture Herglotz wave function*. Abusing the definition slightly, we refer to the limited aperture Herglotz wave function simply as the Herglotz wave function. The Herglotz wave function is an entire solution to the Helmholtz equation.

The next lemma relates the far field due to scattering from an incident Herglotz wave function to the far field due to scattering from incident plane waves. This formalizes the principle of superposition for far field patterns and motivates the numerical techniques we study.

LEMMA 1.1 (superposition of far field patterns). *Let $g \in L^2(-\Lambda)$. Then the solution to the scattering problem for the incident wave*

$$(1.7) \qquad v^i(x) = (Hg)(x), \quad x \in \mathbb{R}^m,$$

is given by

$$v^s(x) = \int_\Lambda u^s(x, -d)g(-d)ds(d), \quad x \in \mathbb{R}^m \backslash \overline{\Omega},$$

and has the far field pattern

$$(1.8) \qquad v^\infty(\hat{x}) = (F_\Omega g)(\hat{x}), \quad \hat{x} \in \mathbb{S}.$$

Proof. Representing the total field v as a boundary integral via [4, Eq.(3.25)] with a density satisfying [4, Eq.(3.26)], the result follows from the linearity and boundedness of the scattering map $u^i \mapsto u^s$. □

LIMITED APERTURE INVERSE SCATTERING. The *inverse problem* we consider is to reconstruct all or part of the boundary $\partial\Omega$ of the scatterer Ω given the incident field u^i and the far field data restricted to the aperture, $u^\infty|_\Lambda$. Let $\Omega_a \subset \mathbb{R}^m$ be a second domain with the same properties as Ω. Denote the operator H restricted to $\partial\Omega_a$ by

$$H_{\partial\Omega_a} := H|_{\partial\Omega_a}.$$

The adjoint of $H_{\partial\Omega_a} : L^2(\Lambda) \to L^2(\partial\Omega_a)$ is denoted $H^*_{\partial\Omega_a} : L^2(\partial\Omega_a) \to L^2(\Lambda)$ and is given by

$$(H^*_{\partial\Omega_a}\psi)(d) := \int_{\partial\Omega_a} e^{-i\kappa x \cdot (-d)}\psi(x)\, ds(x), \ \ d \in \Lambda.$$

If $H_{\partial\Omega_a}$ is injective and has dense range, then with a given density g we can get arbitrarily close to any convenient incident field v^i on $\partial\Omega_a$. Moreover we can construct a mapping from the measured far field pattern to some far field pattern v^∞ that we know more about, and, presumably, can use to find parts of the unknown boundary $\partial\Omega$. Indeed, we can choose v^i, parameterized by some point z, such that $v^\infty(\hat{x}, z) = u^s(z, \hat{x})$. In this way we can reconstruct the scattered field due to an incident field with direction $\hat{x}$ and use this to construct parts of the boundary.

2. The point source method for limited aperture. The fundamental solution $\Phi(\cdot, z)$ and the plane wave $e^{-ik\hat{x} \cdot z}$ are dual to each other in the sense that the far field of the fundamental solution Φ^∞ is given by $\Phi^\infty(\hat{x}, z) = \gamma e^{-ik\hat{x} \cdot z}$, where γ is a constant scaling factor. We use this duality to motivate the point source method. First note that, for incident fields due to point sources $\Phi(\cdot, z)$ with source point located *within* the obstacle, $z \in \Omega$, the scattered wave $w^s(\cdot, z)$ is given by $-\Phi(\cdot, z)$, and thus the far field pattern is given by $-\Phi^\infty$. Secondly, for $\overline{\Omega} \subset \Omega_a$, a straight forward argument using Green's theorem and the boundary conditions for the fields u and w (see [8]) shows that

$$(2.1) \qquad w^\infty(\hat{x}, z) = \gamma u^s(z, -\hat{x}), \ \ \hat{x} \in \mathbb{S}, \ z \in \mathbb{R}^m \backslash \overline{\Omega}_a,$$

or, in words, the scattered field at a point $z \in \mathbb{R}^m \backslash \overline{\Omega}_a$ due to an incident plane wave with direction $-\hat{x}$, $u^s(z, -\hat{x})$, is proportional to the far field at the point $\hat{x}$ due to an

incident point source located at z, $w^\infty(\hat{x}, z)$. This is referred to as the *mixed reciprocity relation* and is discussed in further detail in [11, Theorem 2.1.4]. By *scanning* a region with some approximating domain Ω_a we can put the above facts together not only to locate the boundary $\partial\Omega$ as the points z where $w^\infty(\cdot, z) + \Phi^\infty(\cdot, z) = 0$, but also to reconstruct the scattered field on some region $\mathbb{E}$ outside of Ω.

Placing point sources in some medium around a buried object in order to detect it is tantamount to digging the object up. The next theorem shows us how to do this *virtually* by approximating the far field pattern for scattering due to point sources with the far field pattern for scattering from incident plane waves.

APPROXIMATION OF POINT SOURCES BY PLANE WAVES. In order to construct from plane waves any convenient incident wave, we first must show that the Herglotz wave operator restricted to $\partial\Omega_a$ is injective with dense range.

LEMMA 2.1 (Denseness of restricted Herglotz wave operators). *Assume that κ^2 is not a Dirichlet eigenvalue of the negative Laplacian $-\triangle$ for the domain Ω_a. Then the operators $H_{\partial\Omega_a}$ and $H^*_{\partial\Omega_a}$ are injective and have dense range.*

Proof. Our proof is modeled after similar proofs for the full aperture case [4] and [11]. We first show injectivity of $H_{\partial\Omega_a}$. The Herglotz wave function Hg with $(H_{\partial\Omega_a}g)(x) = 0$ on $\partial\Omega_a$ uniquely solves the Helmholtz equation in Ω_a with zero boundary values. Thus by the assumptions on κ, $Hg = 0$ on the interior of Ω_a. Moreover, since Hg is an *entire* solution to the Helmholtz equation, $Hg = 0$ on all of $\mathbb{R}^m$ and thus, extending g to $\mathbb{S}$ by zero and applying [4, Theorem 3.15], $g = 0$. This proves the injectivity of $H_{\partial\Omega_a}$ and by

$$(2.2) \qquad \overline{H^*_{\partial\Omega_a}(L^2(\partial\Omega_a))} \;=\; N(H_{\partial\Omega_a})^\perp \;=\; L^2(\Lambda)$$

the denseness of the range of $H^*_{\partial\Omega_a}$.

Next, we assume that some density $\varphi \in L^2(\partial\Omega_a)$ satisfies $H^*_{\partial\Omega_a}\varphi = 0$ on Λ. By analytic continuation, this function vanishes on all of $\mathbb{S}$. It can be shown (c.f. [4], Theorem 2.5) that, for the single-layer potential

$$(\tilde{S}\varphi)(x) \;:=\; \int_{\partial\Omega_a} \Phi(x, y)\varphi(y)\, ds(y), \;\; x \in \mathbb{R}^m,$$

the far field pattern is given by $\gamma H^*_{\partial\Omega_a}\varphi$. Thus $\tilde{S}\varphi$ has vanishing far field pattern and by Rellich's Lemma we conclude that $\tilde{S}\varphi := 0$ in $\mathbb{R}^m \setminus \overline{\Omega}$. Now we proceed as in the literature cited above using the jump relations for the single-layer potential, the uniqueness of the interior Dirichlet problem for the Helmholtz equation in Ω_a and the jump relations for the normal derivative of the single-layer potential to derive $\varphi = 0$. This yields uniqueness of $H^*_{\partial\Omega_a}$ and from the equation Eq.(2.2) with the roles of $H_{\partial\Omega_a}$ and $H^*_{\partial\Omega_a}$ interchanged we obtain the denseness of the range of $H_{\partial\Omega_a}$. $\qquad\square$

We are now ready to state the main result that justifies the point source method.

THEOREM 2.1 (Far field patterns of incident point sources). *Let $\Omega_a \subset \mathbb{R}^m$ be a second domain with the same properties as Ω and let $z \in \mathbb{R}^m \setminus \overline{\Omega}_a$. Assume that $\Omega \subset \Omega_a$. Given any $\epsilon > 0$, there exists a $c > 0$ such that, for all $g_*(\cdot, z) \in L^2(-\Lambda)$ satisfying*

$$(2.3) \qquad \|\Phi(\cdot, z) - Hg_*\|_{C(\partial\Omega_a)} \le \epsilon,$$

we have

$$(2.4) \qquad |u^s(z, \hat{y}) - (\mathcal{A}_{\Omega_a}u^\infty)(z, \hat{y})| < c\epsilon, \quad z \in \mathbb{R}^m \setminus \overline{\Omega}_a, \;\; \hat{y} \in \mathbb{S},$$

where

$$(2.5) \qquad (\mathcal{A}_{\Omega_a}\psi)(z,\hat{y}) := \frac{1}{\gamma}\int_\Lambda \psi(d,\hat{y})g_*(-d,z)ds(d).$$

Proof. Let v be a solution to the scattering problem on Ω with $v^i(x) = (Hg_*)(x)$, $x \in \mathbb{R}^m$, where g_* satisfies Eq.(2.3). Then v^i is a Herglotz wave function, and both v^i and Φ solve Eq.(1.1) on the interior of Ω_a. Thus there is a constant $c' > 0$ such that

$$\|\Phi(\cdot,z) - v^i\|_{C(\overline{\Omega}_a)} \le c'\epsilon$$

and hence

$$\|\Phi(\cdot,z) - v^i\|_{C(\partial\Omega)} \le c'\epsilon.$$

On $\partial\Omega$ $v^i = -v^s$ and $w^s(\cdot,z) = -\Phi(\cdot,z)$ where w^s is defined by Eq.(1.6). Thus, since $v^s|_{\partial\Omega} \mapsto v^\infty$ is a continuous mapping $C(\Omega) \to C(\mathbb{S})$, there exists a constant $c^\infty > 0$ such that $\|w^s(\cdot,z) - v^s\|_{C(\partial\Omega)} \le c'\epsilon$ implies

$$|w^\infty(\hat{y},z) - v^\infty(\hat{y})| \le c^\infty c'\epsilon, \quad \forall\, \hat{y} \in \mathbb{S}.$$

By Lemma 1.1, $v^\infty = F_\Omega g_*$. Now, the mixed reciprocity relation Eq.(2.1) together with the standard reciprocity relation $u^\infty(\hat{y},d) = u^\infty(-d,-\hat{y})$ (see [4, Theorem 3.13]) yield the result

$$\left| u^s(z,-\hat{y}) - \frac{1}{\gamma}\int_\Lambda u^\infty(d,-\hat{y})g_*(-d,z)ds(d) \right| \le c^\infty c'\epsilon.$$

$\square$

The operator $\mathcal{A}_{\Omega_a}$ in Eq.(2.5) defines a *back projection* operator, mapping the far field at a point $d \in \Lambda$ due to scattering of a single incident plane wave u^i with direction $-\hat{x}$ from sound-soft obstacle Ω to the scattered field at the point $z \in \mathbb{R}^m\setminus\overline{\Omega}$. Note also that now the signs have a natural interpretation: the scattered field at z due to an incident field with direction $-\hat{x}$ is calculated directly by applying the backprojection operator $\mathcal{A}_{\Omega_a}$ to the corresponding far field on the limited aperture Λ where u^∞ is measured.

APPROXIMATION OF THE SCATTERED FIELD AND THE ILLUMINATED AREA. By Lemma 2.1, if κ is not an eigenvalue of the negative Laplacian on Ω_a, then the set of densities satisfying Eq.(2.3) is nonempty. We can stably calculate g_* and thus the scattered field via Eq.(2.4). In our numerical experiments we calculate the standard Tikhonov regularized estimate

$$(2.6) \qquad g_\alpha(\cdot,z) := (H^*_{\partial\Omega_a}H_{\partial\Omega_a} + \alpha I)^{-1}H^*_{\partial\Omega_a}\Phi(\cdot,z).$$

Using this, we explicitly calculate the approximation $u^s_\alpha(z,-\hat{x}) \approx u^s(z,-\hat{x})$, where

$$(2.7) \qquad u^s_\alpha(z,-\hat{x}) := \frac{1}{\gamma}\int_{-\Lambda} u^\infty(-d,-\hat{x})g_\alpha(d,z)\,ds(d).$$

The procedure sketched above for approximating the scattered field presents us with two challenges. First, for the inverse problem we do not know the location
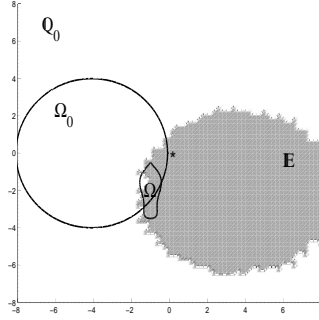
FIG. 2.1. *Scatterer Ω, domain of interest $\mathbb{Q}$, domain of approximation Ω_0 centered on the origin (denoted by $*$), and illuminated area $\mathbb{E}$.*

of Ω, thus we do not know how to construct Ω_a. Second, solving Eq.(2.6)-Eq.(2.7) for every $z \in \mathbb{R}^m$ could be quite expensive. Below we present efficient techniques for meeting these challenges. We take advantage of an analog to the Fourier Shift Theorem to perform these calculations quickly and efficiently without any knowledge of the location of Ω. We focus on these techniques next.

Denote some general area of interest (the computational domain, for example) by $\mathbb{Q}$ where $\Omega \subset \mathbb{Q}$. In principle, the way we find Ω is by scanning some general area $\mathbb{Q}$ that we know satisfies $\Omega \subset \mathbb{Q}$ with an approximation domain Ω_a that we hope is large enough to contain Ω. The quickest way to perform such a scan is by translations of a fixed approximation domain Ω_0,

$$(2.8) \qquad\qquad \Omega_z := z + \Omega_0.$$

Here Ω_0 is a domain with $0 \notin \overline{\Omega}_0$. Let $g_\alpha(x, 0) \in L^2(\Lambda)$ be given by Eq.(2.6) with the point source $\Phi(\cdot, 0)$ and domain of approximation Ω_0. Since Φ is spatially invariant, that is $\Phi(x, z) = \Phi(x - z) = \Phi(x - z, 0)$, then it can be shown that this, together with the identity $(H_{\partial \Omega_a} g)(x - z) = \left[H_{\partial \Omega_a}(e^{-i\kappa z \cdot (\cdot)} g(\cdot)) \right](x)$, yields

$$(2.9) \qquad\qquad g_\alpha(d, z) := e^{-i\kappa z \cdot d} g_\alpha(d, 0), \quad d \in -\Lambda.$$

This is an analog of the Fourier Shift Theorem. Thus, to obtain $u_\alpha^s(z)$ we need only calculate Eq.(2.6) at the point $z = 0$. The integral in Eq.(2.7) is a simple scalar integral and is very easy to calculate for all points z. With this, the backprojection operator $\mathcal{A}_{\Omega_z}$, defined by Eq.(2.5) for domain of approximation Ω_z defined by Eq.(2.8), is efficiently approximated by $(\mathcal{A}_{\Omega_z} \psi)(z, \hat{x}) \approx (\mathcal{A}_\alpha \psi)(z, \hat{x})$ where

$$(2.10) \qquad (\mathcal{A}_\alpha \psi)(z, \hat{x}) := \frac{1}{\gamma} \int_\Lambda \psi(d, \hat{x}) e^{-i\kappa z \cdot (-d)} g_\alpha(-d, 0) \, ds(d), \quad z \in \mathbb{Q}.$$

The function $u_\alpha^s(\cdot, -\hat{x}) = (\mathcal{A}_\alpha u^\infty)(\cdot, -\hat{x})$ is a valid approximation to the scattered field u^s at all points $z \in \mathbb{E}$ where

$$(2.11) \qquad\qquad \mathbb{E} := \{ z \in \mathbb{Q} : \Omega \subset \Omega_z \},$$

i.e. where the unknown scatterer is a subset of the domain of approximation Ω_z. We call $\mathbb{E}$ the *illuminated area*. Values for the magnitude of the field calculated by the point source method at points outside of $\mathbb{E}$ are arbitrarily large – that is, we cannot
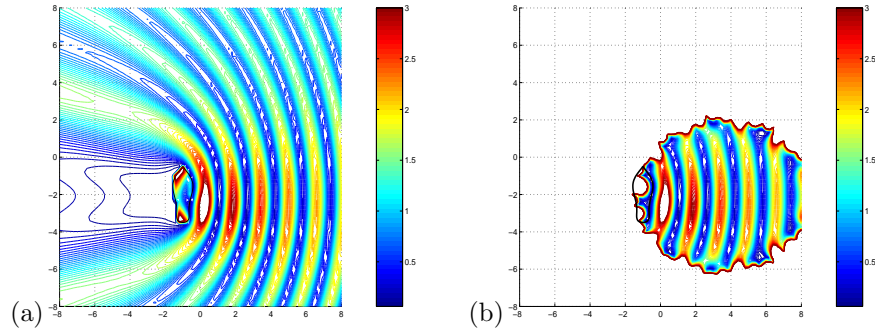
FIG. 2.2. *Contour plot of the magnitude squared of the fields u (a), u_α (b) and the unknown object Ω. The circle around the obstacle in (b) indicates the extent of the aperture. Here, we used the parameters wave number $\kappa = 2$, regularization in Eq.(2.6) of $\alpha = 10^{-12}$, and an incident wave with direction $d = (-1, 0)$. For the domain of approximation Ω_0 we use a large circle with radius $R = 4$ and center $(-4.1, 0)$ shown in Figure 2.1. The illuminated area can clearly be seen in the right image and corresponds to the illuminated area shown also in Figure 2.1*

say what the behavior of u_α^s is on $\mathbb{R}^m \setminus \mathbb{E}$. In practice, the dynamic range of pixel values calculated with the point source method is large, thus a thresholding operation is required in order to see any image features at all. We observe that $|u_\alpha| = |u^i + u_\alpha^s|$, on $\mathbb{Q} \setminus \mathbb{E}$, is *typically* (though not always) large. This being the case, the domain of illumination is found by searching for areas of the domain of interest $\mathbb{Q}$ where the magnitude of the field is smaller than some constant $c > 0$. This constant is estimated by trial-and-error.

THE POINT SOURCE METHOD FOR DOMAIN RECONSTRUCTIONS. Finally, from the reconstructed total field u_α we reconstruct the boundary of the sound-soft scatterer. The field u satisfies Eq.(1.1) with $f = 0$ in Eq.(1.2), thus the natural first step is to simply plot the contours of the magnitude of u_α in a neighborhood of zero. A typical contour plot for full aperture, $\Lambda = \mathbb{S}$ is shown in Figure 2.2. The image in Figure 2.2 only shows pixel values below a certain arbitrarily chosen cut-off. This yields the irregular domain of illumination shown in the figure. The domain of illumination is not known before hand since it depends not only on the domain of approximation Ω_a but also on the obstacle Ω.

3. Image Processing. As we can see from Figure 2.2, direct application of the point source method yields many "minima". The reconstructed total field u_α on the domain $\mathbb{Q}$ approximates the true total field u on the illuminated area $\mathbb{E}$, but, since we do not know Ω at the beginning of the reconstruction, the set $\mathbb{E}$ is not known. Also, in the set $\mathbb{Q} \setminus \mathbb{E}$ in general we do not know how u_α behaves thus we cannot immediately distinguish between artifacts and true minima. In this section we introduce strategies for processing the image in order to extract the *correct* minima from which one can reconstruct the boundary of the unknown object.

There is no substitute for an abundance of good data. Our main goal is not only to manipulate the reconstructed fields to yield more accurate boundary reconstruction, but to compensate for poor and incomplete information by *synthesizing* data sets taken from several different directions and at several different frequencies. From this point forward we denote explicitly the dependence of the fields on the direction of incidence

$d \in \mathbb{S}$ and the frequency $\kappa \in (0, \infty)$ by writing $u^i(\cdot, d, \kappa)$, $u^s(\cdot, d, \kappa)$, $u(\cdot, d, \kappa)$ and $u^\infty(\cdot, d, \kappa)$ for the incident, scattered, total and far fields respectively.

For simplicity, we restrict our attention to two dimensional scattering

$$\mathbb{R}^m = \mathbb{R}^2.$$

We assume that a sampled version of some function ψ is given on a grid $\mathcal{G}$, a partition of the interval $[a_1, b_1] \times [a_2, b_2]$ into $N_1 \times N_2$ equal subintervals. Let $\boldsymbol{n} = (n_1, n_2)$ be a multi-index and denote the corresponding index set by

$$\mathcal{N} = \{\boldsymbol{n} \mid n_1 \in \{0, 1, \cdots, N_1\}, \ n_2 \in \{0, 1, \cdots, N_2\}\}.$$

Denote the point x corresponding to the $\boldsymbol{n}$th grid point by

$$(3.1) \qquad x_{\boldsymbol{n}} \ = \ \left(a_1 + n_1 * \frac{(b_1 - a_1)}{N_1 - 1}, a_2 + n_2 * \frac{(b_2 - a_2)}{N_2 - 1}\right), \quad \boldsymbol{n} \in \mathcal{N}.$$

We write $\psi(\boldsymbol{n})$ for the function ψ sampled at the point $x_{\boldsymbol{n}}$.

We consider two different approaches that are distinguished by the way the sampled function ψ is defined:

$$(3.2) \qquad \psi_{(j,k)}(\boldsymbol{n}) := |u_\alpha(x_{\boldsymbol{n}}, d_j, \kappa_k)|^2,$$

or

$$(3.3) \qquad \psi_j(\boldsymbol{n}) := \left(\sum_k |u_\alpha(x_{\boldsymbol{n}}, d_j, \kappa_k)|^2\right)^{-1}.$$

In the first instance ψ is the *intensity* of the total field (i.e. the square of the modulus) due to a single frequency incident field with frequency κ_k and direction d_j. Here we explicitly denote the dependence of the fields on the direction of incidence and the frequency. In the second instance, Eq.(3.3), the data is the *inverse intensity* of the total field of a *polychromatic* incident field with direction direction d_j. This approach is a multiple frequency version of the metric used in the linear sampling and MUSIC algorithms for imaging extended objects [2].

Regardless of the definition of ψ_j, we gather several such images, each distinguished by either the frequency κ at which the image was generated, or the direction of the incident field, $\tilde{d}$, or by both. The direction $\tilde{d}$ is determined by the aperture. Define the aperture $\Lambda \subset \mathbb{S}$ by

$$(3.4) \qquad \Lambda(\theta, d) \ := \ \left\{\tilde{d} \in \mathbb{S} \ \middle| \ \tilde{d} \cdot d \geq \cos(\theta/2)\right\}$$

with angle $\theta \in (0, 2\pi)$ and direction $d \in \mathbb{S}$. For simplicity, we consider only incident waves with direction $\tilde{d}$ opposite that of the radial axis of the aperture $\Lambda(\theta, d)$, that is $d = \tilde{d}$. The heuristic reason for this is that, regardless of the direction of the axis of the aperture $\Lambda(\theta, d)$, the most informative data is that corresponding to backscattering, $\tilde{d} = -d$. Together the direction of the aperture axis and the direction of the incident wave are called the *view* and are designated by the direction of the axis of the aperture, d.

In the case of single frequency imaging defined by Eq.(3.2), for a given view d_j we produce images $\psi_{(j,k)}$ with different wave numbers κ_k, $k = 1, ..., K$. We extract the part of the boundary of the obstacle Ω within the illuminated area $\mathbb{E}$ as the minima

that are common to each of the images $\psi_{(j,k)}$. This is repeated for several different views d_j, $j = 1, 2, \ldots, J$, so that, when taken together, the synthesized data sets yield a correct estimate of the boundary. To reduce notational clutter we define the multi-index $\boldsymbol{j} \in \mathcal{J}$ where

$$\mathcal{J} := \{\boldsymbol{j} = (j,k) \mid j \in \{1, 2, \ldots, J\}, \ k \in \{1, 2, \ldots, K\}\}.$$

The vector of images $\psi_{\boldsymbol{j}}$ is indicated with bold-faced type, $\boldsymbol{\psi} \in [\mathbb{R}_+^{N_1} \times \mathbb{R}_+^{N_2}]^{JK}$,

$$(3.5) \qquad\qquad \boldsymbol{\psi} = (\psi_{(1,1)}, \psi_{(1,2)}, \ldots, \psi_{(J,K)})$$

3.1. The point source method and logical image processing.
Since logical image processing involves mappings of sampled function values to either 0 or 1, we denote the binary set $\mathbb{K} = \{0, 1\}$ and thus the binary space corresponding to $\mathbb{R}^{N_1} \times \mathbb{R}^{N_2}$ is $\mathbb{K}^{N_1} \times \mathbb{K}^{N_2}$. For points on the grid, $z \in \mathcal{G}$, we use the 8-neighborhoods

$$(3.6) \qquad \left\{ y \in \mathcal{G} : \ y = z + \left(\xi_1 \frac{(b_1 - a_1)}{N_1 - 1}, \xi_2 \frac{(b_2 - a_2)}{N_2 - 1} \right) \text{ for } \xi_1, \xi_2 \in \{-1, 0, 1\} \right\}$$

We call a set of points $U \subset \mathcal{G}$ *connected*, if for any two points $z_{\boldsymbol{1}}, z_{\boldsymbol{2}} \in U$ there is a sequence $y_{\boldsymbol{1}}, \ldots, y_{\boldsymbol{n}}$ of points such that $y_{\boldsymbol{1}} = z_{\boldsymbol{1}}$, $y_{\boldsymbol{n}} = z_{\boldsymbol{2}}$ and $y_{\boldsymbol{j+1}}$ is in a 8-neighborhood of $y_{\boldsymbol{j}}$ for $\boldsymbol{j} = \boldsymbol{1}, \ldots, \boldsymbol{n} - \boldsymbol{1}$. Usually, the subsets of $\mathcal{G}$ are mapped bijectively onto the set of binary images on $\mathcal{G}$ where a subset $U \subset \mathcal{G}$ is identified with the binary image ψ that has values $\psi(z) = 1$ for all $z \in U$ and $\psi(z) = 0$ for all $z \in \mathcal{G} \setminus U$.

GLOBAL MINIMA. First, we search for small function values. This is performed by the *binary thresholding operator* $\mathcal{T}_0 : \mathbb{R}_+^{N_1} \times \mathbb{R}_+^{N_2} \to \mathbb{K}^{N_1} \times \mathbb{K}^{N_2}$ defined by

$$(3.7) \qquad\qquad (\mathcal{T}_0 \psi)(\boldsymbol{n}) := \begin{cases} 1, & \psi(\boldsymbol{n}) < \delta, \\ 0, & \text{otherwise}, \end{cases}$$

for $\boldsymbol{n} \in \mathcal{N}$, where $\delta > 0$ is some *threshold parameter*.

LOCAL MINIMA. Alternatively, we could search for local minima, which is of some advantage when the data is corrupted by large error and the 'true' minimum at the boundary has larger values than the minima of the wave far from the boundary. The extraction of local minima in direction $(1, 0)$ is accomplished by applying $\mathcal{T}_1 : \mathbb{R}_+^{N_1} \times \mathbb{R}_+^{N_2} \to \mathbb{K}^{N_1} \times \mathbb{K}^{N_2}$,

$$(3.8) \qquad (\mathcal{T}_1 \psi)(\boldsymbol{n}) := \begin{cases} 1, & \psi(n_1 - 1, n_2) > \psi(\boldsymbol{n}), \text{ and } \psi(n_1 + 1, n_2) > \psi(\boldsymbol{n}); \\ 0, & \text{otherwise}. \end{cases}$$

The operator $\mathcal{T}_2$ corresponding to the local minimum in the direction $(0, 1)$ is defined analogously.

REMOVAL OF ISOLATED NOISE. Next, we include some knowledge about the unknown obstacle to narrow the number of possible minima. The boundary Γ of the obstacle is a connected set where we expect some length of the boundary curve. Therefore, we remove all minima that appear in some sense *isolated*. For parameters $\rho_2 > \rho_1 > 0$ we define the removal operator $\mathcal{T}_3 : \mathbb{K}^{N_1} \times \mathbb{K}^{N_2} \to \mathbb{K}^{N_1} \times \mathbb{K}^{N_2}$ by

$$(3.9) \qquad (\mathcal{T}_3 \psi)(\boldsymbol{n}) := \begin{cases} 1, & \psi(\boldsymbol{n}) = 1 \text{ and } \exists x_{\mathbf{m}} \in \mathcal{G} \text{ with} \\ & \rho_2 \geq d(x_{\mathbf{m}}, x_{\boldsymbol{n}}) \geq \rho_1 \text{ and } \psi(x_{\mathbf{m}}) = 1 \\ 0, & \text{otherwise}, \end{cases}$$

for $\boldsymbol{n}, \mathbf{m} \in \mathcal{N}$. Here $d(x_{\mathbf{m}}, x_{\boldsymbol{n}})$ is the distance between the points $x_{\mathbf{m}}$, and $x_{\boldsymbol{n}}$.

FIXED VIEW AND LOGICAL 'AND'. In the case of single frequency images defined by Eq.(3.2), for a fixed view, d_j, to find the minima common to all the images $\psi_{\boldsymbol{j}}$ gathered at different frequencies κ_k we introduce the logical &. Define the operator $\mathcal{T}_4 : [\mathbb{K}^{N_1} \times \mathbb{K}^{N_2}]^K \to \mathbb{K}^{N_1} \times \mathbb{K}^{N_2}$ by

$$(3.10) \qquad (\mathcal{T}_4 \boldsymbol{\psi})(\boldsymbol{n}) \;:=\; \psi_{\boldsymbol{j}_1}(\boldsymbol{n}) \; \& \; ... \; \& \; \psi_{\boldsymbol{j}_K}(\boldsymbol{n}),$$

for $\boldsymbol{j}_k = (j, k) \in \mathcal{J}$ (j fixed), with the logical operator & that produces 1 only if all arguments are 1 and 0 otherwise.

MULTIPLE VIEWS AND LOGICAL 'OR'. For multiple views d_j introduce the *or* operator $\mathcal{T}_5 : [\mathbb{K}^{N_1} \times \mathbb{K}^{N_2}]^J \to \mathbb{K}^{N_1} \times \mathbb{K}^{N_2}$ by

$$(3.11) \qquad (\mathcal{T}_5 \boldsymbol{\psi})(\boldsymbol{n}) \;:=\; \psi_{\boldsymbol{j}_1}(\boldsymbol{n}) \; | \; ... \; | \; \psi_{\boldsymbol{j}_J}(\boldsymbol{n}),$$

for $\boldsymbol{j}_j = (j, k) \in \mathcal{J}$, with $\boldsymbol{\psi}$ given by Eq.(3.5) and the logical operator | that produces 1 if one of the arguments is 1 and 0 otherwise. Alternatively, we might use an arithmetic sum of the images and a thresholding operator afterwards.

MASKING OPERATIONS. The masking operation uses the knowledge about the illuminated area. For each image and each minimum point in this image remove all minima points from the other images that are located in a translated cone $y + \mathbb{V}$ with $\mathbb{V}$ given by

$$(3.12) \qquad \mathbb{V}(d, \phi) = \left\{ x \in \mathbb{R}^2 \; | \; x \cdot d \geq |x| \cos(\phi). \right\}$$

Here $d \in \mathbb{S}$ is the corresponding image observation direction, $y \in \mathbb{R}^2$ the current minimum pixel and $\phi \in [0, \pi/2]$ some prescribed opening angle.

3.2. Image synthesis via averaging. The & and | operations detailed above, together with the masking and thresholding operations, are boolean versions of the weighted averaging strategies discussed next.

Given the linear operators $\mathcal{M}_{\boldsymbol{j}} : \mathbb{R}^{N_1} \times \mathbb{R}^{N_2} \to \mathbb{R}^{N_1} \times \mathbb{R}^{N_2}$ and images $\psi_{\boldsymbol{j}} \in \mathbb{R}_+^{N_1} \times \mathbb{R}_+^{N_2}$, we seek a function $\varphi \in \mathbb{R}^{N_1} \times \mathbb{R}^{N_2}$ satisfying

$$(3.13) \qquad \mathcal{M}_{\boldsymbol{j}} \varphi = \psi_{\boldsymbol{j}}, \quad \forall \boldsymbol{j} \in \mathcal{J},$$

where $\mathcal{J}$ is the index set of images defined above. Our situation is no different from most practical applications in that a solution to Eq.(3.13) does not exist. Notwithstanding noise, each view d_j will generate an image that cannot possibly match the images from other views because of the limited illuminated area $\mathbb{E}$. We thus seek a "best fit" to for the system Eq.(3.13) given some *performance measure*, $\rho : \left[\mathbb{R}^{N_1} \times \mathbb{R}^{N_2} \right]^{JK} \to \mathbb{R}$. Also, in many applications the operators $\mathcal{M}_{\boldsymbol{j}}$ do not have a bounded inverse from $\mathbb{R}^{N_1} \times \mathbb{R}^{N_2}$ to $\mathbb{R}^{N_1} \times \mathbb{R}^{N_2}$. To allow for this, we employ regularization strategies for the problem of finding an optimal solution to the general problem

$$(3.14) \qquad \text{minimize } \rho \left(\boldsymbol{\psi} - \boldsymbol{\mathcal{M}} \varphi \right) + \widetilde{\alpha} f(\varphi)$$
$$\text{over} \quad \varphi \in \mathbb{R}^{N_1} \times \mathbb{R}^{N_2}.$$

where $\boldsymbol{\psi} \in \left[\mathbb{R}_+^{N_1} \times \mathbb{R}_+^{N_2}\right]^{JK}$ is the vector of functions $\psi_{\boldsymbol{j}}$, $\boldsymbol{\mathcal{M}} : \mathbb{R}^{N_1} \times \mathbb{R}^{N_2} \to \left[\mathbb{R}^{N_1} \times \mathbb{R}^{N_2}\right]^{JK}$ is the vector of mappings $\mathcal{M}_{\boldsymbol{j}}$, and $f : \mathbb{R}^{N_1} \times \mathbb{R}^{N_2} \to \mathbb{R}$ is some regularization mapping to stabilize the solution with respect to small variations in the data $\psi_{\boldsymbol{j}}$. The regularization parameter $\widetilde{\alpha} \in \mathbb{R}_+$ is not to be confused with the regularization parameter associated with the calculation of the Herglotz wave function g_α Eq.(2.6).

Any type of performance measure ρ is possible, each giving a different solution φ. Likewise, the regularization term $f(\varphi)$ can be chosen with some flexibility. The most common regularized performance measure – the one we consider here – is the Tikhonov regularized least squares measure[2]

(3.15)
$$\text{minimize} \sum_{\boldsymbol{j}} \beta_{\boldsymbol{j}} \|\psi_{\boldsymbol{j}} - \mathcal{M}_{\boldsymbol{j}} \varphi\|^2 \; + \; \widetilde{\alpha}^2 \|\varphi\|^2$$

$$\text{over} \quad \varphi \in \mathbb{R}^{N_1} \times \mathbb{R}^{N_2}.$$

One advantage of the Tikhonov regularized least squares measure is that the optimal solution to Pr.(3.15), φ_*, can be written down in closed form as the solution to the normal equations

(3.16)
$$\varphi_* = \left[\sum_{\boldsymbol{j}} \beta_{\boldsymbol{j}} \mathcal{M}_{\boldsymbol{j}}^* \mathcal{M}_{\boldsymbol{j}} + \widetilde{\alpha}^2\right]^{-1} \sum_{\boldsymbol{j}} \beta_{\boldsymbol{j}} \mathcal{M}_{\boldsymbol{j}}^* \psi_{\boldsymbol{j}},$$

where $\boldsymbol{j} \in \mathcal{J}$ and $\mathcal{M}_{\boldsymbol{j}}^*$ is the adjoint of $\mathcal{M}_{\boldsymbol{j}}$. This formulation yields some very old and familiar techniques.

EXAMPLE 3.1. :

(i) (weighted average) If $\mathcal{M}_{\boldsymbol{j}} = \mathcal{I}$ for all $\boldsymbol{j} \in \mathcal{J}$, then from Eq.(3.16) we have

(3.17)
$$\varphi_* = \frac{1}{\sum_{\boldsymbol{j}} \beta_{\boldsymbol{j}} + \widetilde{\alpha}^2} \sum_{\boldsymbol{j}} \beta_{\boldsymbol{j}} |u_{\boldsymbol{j}}|^2$$

(i) (filtered weighted average) For $\mathcal{M}_{\boldsymbol{j}}$, $(\boldsymbol{j} \in \mathcal{J})$ a pointwise real multiplication operator, that is $(\mathcal{M}_{\boldsymbol{j}} \varphi)(\boldsymbol{n}) = \mathcal{M}_{\boldsymbol{j}}(\boldsymbol{n}) \varphi(\boldsymbol{n})$, for $\boldsymbol{n} \in \mathcal{N}$, then from Eq.(3.16) we have

(3.18)
$$\varphi_*(\boldsymbol{n}) = \frac{\sum_{\boldsymbol{j}} \beta_{\boldsymbol{j}} \mathcal{M}_{\boldsymbol{j}}(\boldsymbol{n}) |u_{\boldsymbol{j}}(\boldsymbol{n})|^2}{\sum_{\boldsymbol{j}} \beta_{\boldsymbol{j}} \mathcal{M}_{\boldsymbol{j}}^2(\boldsymbol{n}) + \widetilde{\alpha}^2}$$

We discuss specific filters $\mathcal{M}_{\boldsymbol{j}}$ in the next section.

Our numerical demonstrations are generated from simulated data. Since practical applications involve real data, a remark on the performace measure that we consider for image averaging Eq.(3.15) is in order. While the least squares measure is mathematically convenient and therefore common, the performance measure ρ in the general formulation Eq.(3.14) should be consistent with the statistical model for the noise. If $\psi_{\boldsymbol{j}}$ is a realization of a stochastic process with additive zero mean white noise, then

_____

[2]The image averages discussed here are not to be confused with the standard optimization formulation for finding the unknown boundary (see [4, pp.140-144] and references therein). Rather than seeking a function Γ representing the boundary, we seek a function φ that is closest in a least squares sense to the pointwise intensities of the total fields calculated from several far field measurements.

Eq.(3.15) with $\widetilde{\alpha} = 0$ is the negative of the log-likelihood functional of the maximum likelihood estimator of the normal density functional $p(\psi_j; \varphi)$ parametrized by the unknown function φ with variance $1/\sqrt{2M\beta_j}$. Likewise, the regularization term can be interpreted in an information theoretic setting. The penalty $\widetilde{\alpha}\|\varphi\|^2$ is the standard Tikhonov regularization term. It can be shown that in this setting the optimal choice of the parameter $\widetilde{\alpha}$ in a probabilistic sense is the value that corresponds to the spectral density of the noise over all data sets j [6]. With this value of $\widetilde{\alpha}$, the solution to Pr.(3.15) yields the optimal Wiener filter for the image φ. Obviously, ill-posedness of the model Eq.(3.13) is also a factor, and a balance must be struck between noise smoothing and computational stability. If the noise process does not follow Gaussian statistics, then the least squares estimator is not appropriate and other performance measures should be explored, for example, maximum entropy.

4. A numerical study. The test obstacles given below are parameterized by $t \in [0, 2\pi)$. We start with a simple ellipse Ω_1,

$$(4.1) \qquad\qquad x_1 = 0.5 * \cos(t) - 1, \quad x_2 = 1 * \sin(t) - 2.$$

The Object Ω_2 is a boat given by

$$(4.2) \qquad x_1 = 0.5 * \cos(t) + 0.1 * \sin(4 * t)) - y_1, \quad x_2 = 1.5 * \sin(t) - y_2,$$

where $y = (y_1, y_2)$ is a translation parameter. We also tested a non-convex 'kite shaped' object Ω_3 given by

$$(4.3) \qquad x_1 = -1 * (\cos(t) + 0.65 * \cos(2 * t) - 0.65) - 1, \quad x_2 = 1.5 * \sin(t) - 2.$$

The domain of illumination $\mathbb{E}$ for objects $\Omega_1 - \Omega_3$ corresponding to the domain of approximation Ω_0 shown in Figure 2.1 are shown in Figure 4.1.

We study the performance of the point source method in conjunction with the image processing strategies discussed in section 3 on each of the obstacles in several settings. First, we consider the case of one wave, single frequency. Note that the reconstruction of the total field intensity with the limited aperture data in Figure 4.1(e) is not significantly different from the reconstruction using a full 2π aperture shown in Figure 2.2(b). This is typical for our experiments, thus we use the 'moderate' aperture of 0.4π shown here as our reference for all experiments. We also investigate the breakdown in reconstructions as we vary the aperture size from *small aperture,* $\theta = 0.1\pi$ to *very small aperture,* $\theta \leq .02\pi$. We then study the effect of using multiple frequencies for a fixed view. Finally, we study the reconstruction of Ω with multiple views, single and multiple frequency illumination.

4.1. Demonstration of logical image processing. We demonstrate the result of the logical operators for the processing of the images that are obtained from the point source method for limited aperture. We start with results for scattering of a single wave.

First, in Figure 4.2 we show the outcome of thresholding on the reconstructed field corresponding to Figure 4.1(e). The minima of the curve are dynamically located such that the Frobenius norm of the binary output is larger than some prescribed value (we chose 10 for the image with a resolution of 40×40 pixels).

The thresholded version of the images in Figure 4.2(a) shows a large number of artifacts. These artifacts are 'small' in the sense that they are isolated as described by
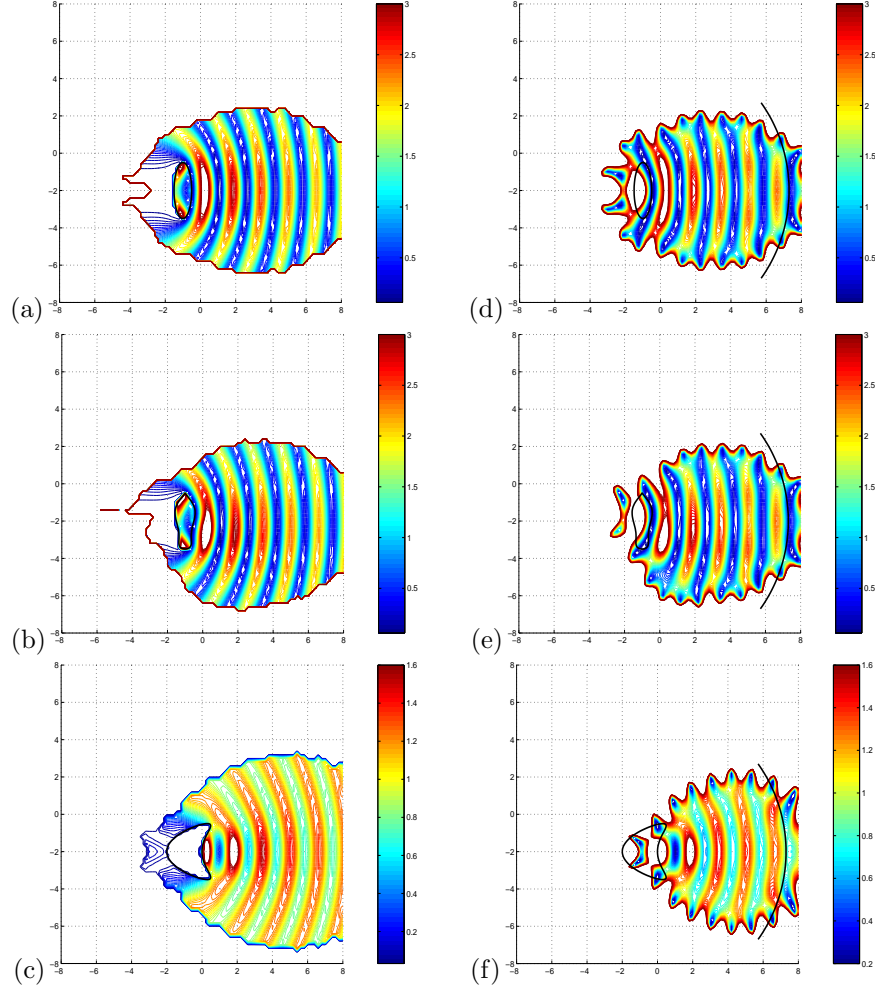
FIG. 4.1. *Frames (a)-(c) show a direct,* forward, *calculation of the intensity of the total field for scattering from a single incident wave by the obstacles* $\Omega_1 - \Omega_3$ *respectively on the domain of illumination* $\mathbb{E}$ *for the reconstructed total fields shown to the right. Frames (d)-(f) show the intensity of the total field reconstructed on* $\mathbb{E}$ *corresponding to the domain of approximation* Ω_0 *shown in Figure 2.1 from 30 far field data samples on a limited aperture. The parameters for all images are wave number* $\kappa = 2$; *aperture opening* $\theta = 0.4 * \pi$; *view* $d = (1, 0)$; *regularization in Eq.(2.6) of* $\alpha = 10^{-12}$.

the operator $\mathcal{T}_3$. We apply the operator $\mathcal{T}_3$ three times, first with $\rho_1 = 1$ and $\rho_2 = 2$, then with $\rho_1 = 2$ and $\rho_2 = 3$ and finally with $\rho_1 = 3$ and $\rho_2 = 4$, each measured in pixels. The result is shown in Figure 4.2(b).

Next, we consider the case of multiple frequencies. We start with a fixed view and choose some waves with different wave numbers, here with $\kappa = 1$, $\kappa = 1.5$ and $\kappa = 2$ and combine the images by the logical operator $\mathcal{T}_4$. The images for the different wave numbers are shown in Figure 4.3. The last image in Figure 4.3 is the result of the logical 'and' as given by the operator $\mathcal{T}_4$. The curve shows only those points which are part of all three preceding images.
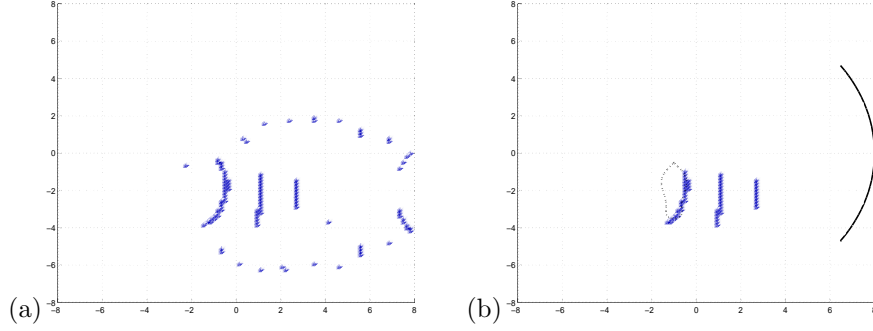
FIG. 4.2. *The image (a) after the application of the operator $\mathcal{T}_0$ with $\delta = 0.4$. The removal step (b) for isolated artifacts obtained by an application of the operator $\mathcal{T}_3$ to the thresholded image. For each we measure the far field at 30 points with the parameters wave number $\kappa = 2$; aperture opening $\theta = 0.4 * \pi$; view $d = (1,0)$; regularization $\alpha = 10^{-12}$.*
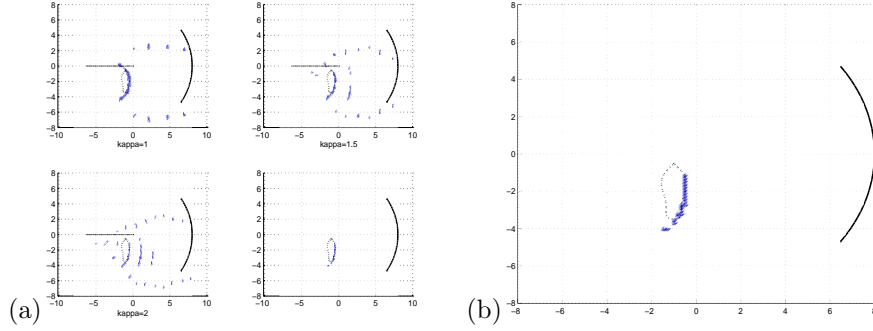

FIG. 4.3. *(a) The first three images shows thresholded reconstructions for fixed view and different wave numbers. The fourth image and an enlarged version in image (b) is obtained by the application of $\mathcal{T}_4$ to the first three images. We use the parameters wave numbers $\kappa = 1$, $\kappa = 1.5$ and $\kappa = 2$; aperture opening $\theta = 0.4 * \pi$; view $d = (1,0)$; regularization $\alpha = 10^{-12}$ for the reconstructions of the obstacle Ω_1. For each frequency we took 30 measurements of the far field pattern.*

By changing both the direction of incidence of the incoming waves and the location of the measurement device we expect more information about the different sides of the object under consideration. The logical operator $\mathcal{T}_5$ has been built to incorporate the additional knowledge by a logical 'or' operation on different images. Figure 4.4 demonstrates the result of the operator $\mathcal{T}_5$ applied to images that have been produced by three different views.

With another image we demonstrate the need for further logical operators, since the operator $\mathcal{T}_5$ keeps some artifacts that can be removed by taking into account more knowledge about the illuminated area of the point source method. In Figure 4.5 we employ a masking operation that removes minima points using the operator $\mathcal{T}_6$ described in section 3.1.

4.2. Demonstration of averaging. The averaging techniques described in section 3.2, complementary to the logical image processing illustrated above, are robust techniques for extracting image features from several data sets. The critical compo-
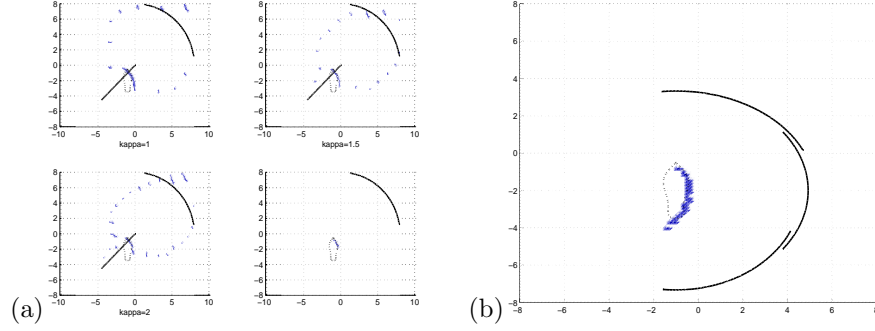
FIG. 4.4.   (a) The image shows the separate reconstruction result for three views, each with three different wave numbers.   (b) The image shows the integrated reconstruction result for three views produced by the logical operator $\mathcal{T}_5$.   In each of these we use the parameters wave numbers $\kappa = 1, 1.5, 2$; aperture opening $\theta = 0.2 * \pi$; views $v = (\sqrt{0.5}, -\sqrt{0.5}), (1, 0), (\sqrt{0.5}, \sqrt{0.5})$; regularization $\alpha = 10^{-7}$ for a reconstruction of the obstacle Ω_1. The far field has been measured at 30 points.
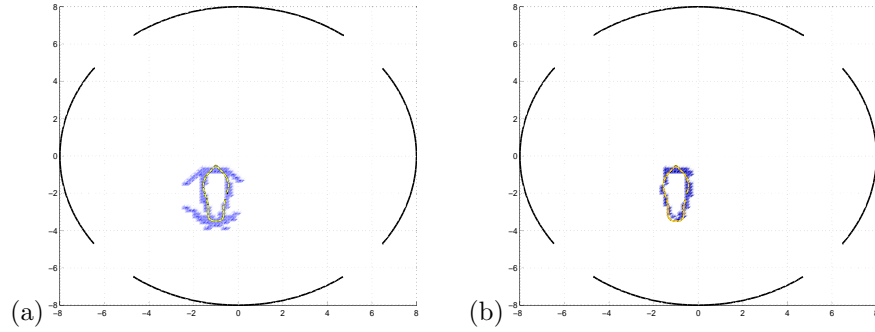
FIG. 4.5. (a) demonstrates artifacts coming from the pure logical summation ('or' operation) of images. For (b) we employ a masking operation as defined by the logical operator $\mathcal{T}_6$ to remove the artifacts. We use the parameters wave numbers $\kappa = 1, \kappa = 1.5, \kappa = 2$; aperture openings $\theta = 0.4 * \pi$; views $v = (0, -1)$, $v = (1, 0)$, $v = (0, 1)$, $v = (-1, 0)$; regularization $\alpha = 10^{-12}$ for a reconstruction of the obstacle Ω_1.

nent of the averaged image prescribed by Eq.(3.16) is the filter $\mathcal{M}_{\boldsymbol{j}}$ and the definition of $\psi_{\boldsymbol{j}}$. This is illustrated with the following examples.

AVERAGING INTENSITIES: SINGLE VIEW. We begin with limited aperture far field data generated from a single incident wave. It is clear from Figure 2.2 that reconstruction of the total field intensity generates many minima in addition to the one at the boundary. To rule out certain possibilities we average the intensities of the total fields over several wavelengths. This simple but effective technique is illustrated in Figure 4.6.

AVERAGING AND FILTERING INTENSITIES: MULTIPLE VIEWS. For the images defined by Eq.(3.2), averaging over several different *views* of the obstacle is not so straight forward. The reason for this is that large uninformative pixel values calculated by the point source method dominate the smaller pixel values of interest. Shown in Figure 4.7(a) is an unfiltered ($\mathcal{M}_{\boldsymbol{j}} = \mathcal{I}$ for all $\boldsymbol{j} \in \mathcal{J}$) average of each of the views calculated
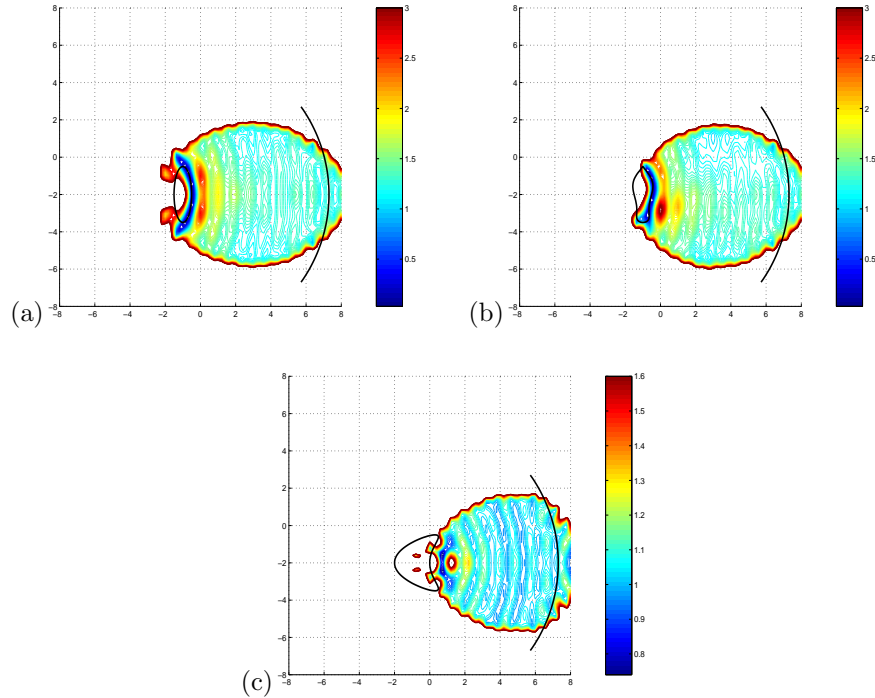
FIG. 4.6.   *Frames (a)-(c) show the average intensity at 9 different wavelengths of the total field reconstructed on the domain of illumination (see Figure 4.1) from 30 far field data samples on a limited aperture with one incident wave direction and 9 different wavelengths.   The parameters for all images are wave numbers $\kappa = .75, 1.0833, 1.4167, 1.75, 2.0833, 2.4167, 2.75, 3.0833, 3.4167, 3.75$; aperture opening $\theta = 0.4 * \pi$; view $v = (1, 0)$; regularization $\alpha = 10^{-12}$.*

via Eq.(3.17). Nearly all information about the obstacle is lost in averaging – but not all. The remaining information allows us to estimate the center of the obstacle. We then use this center information to construct a mask similar to the operator $\mathcal{T}_6$ described in section 3.1 for filtering out the large pixel values outside the domain of illumination. The mask is illustrated in Figure 4.7(c).

To estimate the center of the unknown obstacle, we first calculate the total field for each of the incident wave and view directions. Next, the region $\mathbb{E}$ is estimated by applying a threshold to the calculated intensities for each of the incident fields/views. The intersection of the domains $\mathbb{E}$ is shown in Figure 4.7(b). Without any knowledge of the location of the obstacle, we observe that, when the views are radially symmetric, the geometric center of the *intersection* of the domains of illumination roughly coincides with the geometric center of the obstacle. When the views are not radially symmetric, as is the case when only "one sided" views are possible, we add a constant bias to the calculation of the center of the filter in order to compensate for the asymmetry of the views. For our example, the center of mass of the intersection of all of the domains of illumination is calculated to be $(-3.8, -2.0)$. The true center of the obstacle is at $(-1.0, -2.0)$. Note that the second coordinate is exact, while the first coordinate – the direction of asymmetry – has a significant negative bias.

We use this calculated center of mass as the center of a series of translated *cone masks* shown in Figure 4.7(c). Let $\boldsymbol{n}$ be the pixel location, $\boldsymbol{n}_c$ the center of mass

(in pixels) of the intersection of the domains of illumination, $d_j \in \mathbb{S}$ the vector corresponding to the direction of the view, and let $\phi > 0$ be the opening angle of the cone given by Eq.(3.12). The mask is explicitly given by

$$(4.4) \qquad\qquad \mathcal{M}_{\boldsymbol{j}}(\boldsymbol{n}) = \left\{ \begin{array}{ll} 1 & \text{if } (\boldsymbol{n} - \boldsymbol{n}_c) \in \mathbb{V}(d_j, \phi) \\ 0 & \text{otherwise} \end{array} \right. .$$

In our experiments we choose the opening angle ϕ so that the cone $\mathbb{V}(d_j, \phi)$ has the same opening angle for every direction d_j. These opening angles are chosen large enough so that translated cones from different views overlap slightly as shown in Figure 4.7(c). This in effect oversamples the outer edges of the domains of illumination in an attempt to *match* disjoint regions of the image. The result of applying such a mask to the image average via Eq.(3.18) is shown in Figure 4.7(d). The results for the other objects are shown in Figure 4.7(e)-(f).

INVERSE INTENSITY OF POLYCHROMATIC WAVES. In all of the examples above we have used the data definition given by Eq.(3.2), that is, the intensity of monochromatic waves. This data illustrates dramatically the effect of filtering on image reconstruction. Here, we briefly demonstrate the alternative data definition given by Eq.(3.3), that is, the inverse intensity of polychromatic waves. This change in the data yields tremendous improvements in image quality *without* the use of filters. In Figure 4.8 we show results from 4 views with 9 frequencies.

We emphasize that the results shown in Figure 4.8 are achieved without the use of filters. In our experiments, filtering with the cone mask described in the previous subsection did improve the quality of the reconstructions, but not as dramatically as with the averaged intensities.

4.3. Small aperture, very small aperture, and undersampling the far field. We conclude this section with a demonstration of the breakdown of the procedures outlined above for very small apertures and sparse sampling of the far field. We begin with an illustration of the breakdown in the image reconstruction as the sampling on the aperture is decreased. Figure 4.9 demonstrates the breakdown of the reconstruction when we pass from 15 far field samples to three samples. We show in Figure 4.10 that as the aperture becomes smaller the data in the far field approximates simple backscattering and curvature information in the boundary of the object is lost. Image degradation is noticeable for apertures as small as 0.05π, and by 0.01π much of the fine detail of the obstacle has been lost, although the approximate location and size can still be estimated. The effect of decreasing aperture size on boundary reconstructions from multiple views is also shown in Figure 4.10. For all of these images, the number of samples on the apertures was kept constant at 30 sample points, regardless of the size of the aperture. Finally, in Figure 4.11 we show reconstructions with very small aperture of 0.1 degree, i.e. 0.0006π, 10 far field measurements and three different wave numbers. The location and approximate size of the object can be well reconstructed even with this extremely limited amount of data.

5. Conclusion. The logical and statistical image processing techniques demonstrated above combine different data sets, a theoretical understanding of the mathematical and physical processes behind each data set, and experience to reconstruct an unknown, sound-soft obstacle from several incomplete far-field measurements. Each data set consists of limited aperture measurements of the far field pattern resulting from a single incident excitation. We use the point source method to obtain localized reconstructions of the boundary of the obstacle. We combined the results from several
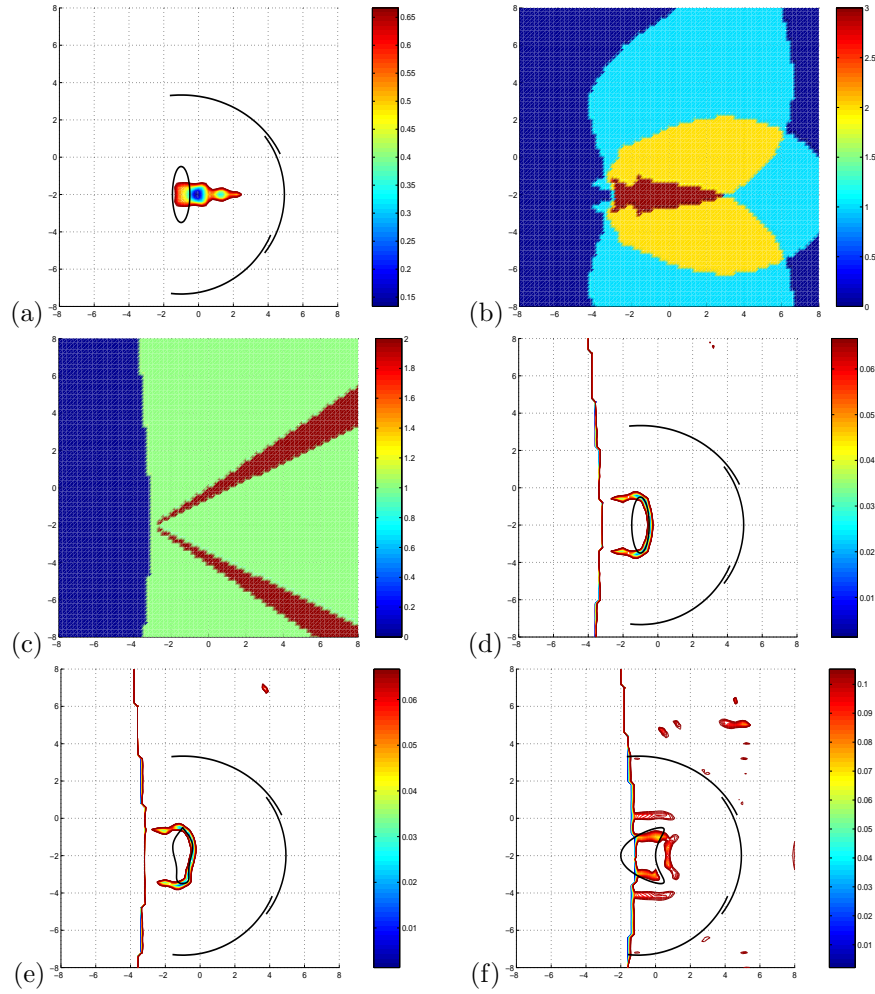
FIG. 4.7. *(a) the unfiltered,* $\mathcal{M}_j = \mathcal{I}$ *for all* $j \in \mathcal{J}$, *average intensity of the far field reconstructed from the far field data sampled at three different directions corresponding to three different incident field directions; (b) the overlapping domains of illumination for all of the three views; (c) the cone mask filter prescribed by Eq.(4.4) for all of the views centered on the center of mass of the intersection of the domains of illumination; (d) the averaged total field intensity calculated via Eq.(3.18). (e)-(f) the averaged total field intensity calculated via Eq.(3.18) with the cone mask given by Eq.(4.4) for obstacles* Ω_2 *and* Ω_3 *respectively. The centers for the masks are calculated separately depending on the center of mass of the intersection of the domains of illumination. The parameters for all images are wave numbers* $\kappa = .75, 1.0833, 1.4167, 1.75, 2.0833, 2.4167, 2.75, 3.0833, 3.4167, 3.75$; *aperture opening* $\theta = 0.4 * \pi$; *views* $v = (1/2, \sqrt{3}/2), (1, 0), (1/2, -\sqrt{3}/2)$; *regularization* $\alpha = 10^{-12}$.

such reconstructions at several frequencies (less than 10) and directions (at most 4) to obtain an estimate of the boundary where possible. In the case of "one sided" views we were only able to reconstruct the corresponding side of the obstacle. For views around the entire obstacle, we were able to obtain a complete estimate of the obstacle. These techniques allow one to reliably reconstruct scatterers from limited and incomplete scattering data. Indeed, we showed that these techniques together yield reasonable boundary estimates with extremely limited amounts of data. This will

greatly facilitate future research employing these techniques in realistic 3 dimensional settings in which a scarcity of data is a major hurdle.

REFERENCES

[1] Brandfass, M., Lanterman, A. D. and Warnick, K. F.: "A comparison of the Colton-Kirsch inverse scattering methods with linearized tomographic inverse scattering." Inverse Problems 17, 1797-1816 (2001).

[2] Cheney, M.: "The linear sampling method and the MUSIC Algorithm." Inverse Problems 17, 591-595 (2001).

[3] Colton, D. and Kirch, A.: "A simple method for solving inverse scattering problems in the resonance region." *Inverse problems* **12**(4), 383-93 (1996).

[4] Colton, D. and Kress, R.: *Inverse Acoustic and Electromagnetic Scattering Theory.* 2nd Ed., Springer-Verlag (1998).

[5] Gilbarg, D. and Trudinger, N.S.: *Elliptic Partial Differential Equations of Second Order* Springer 1998.

[6] A. Jain: *Fundamentals of Digital Image Processing*, Prentice Hall (1989)

[7] Kirch, A: "Characterization of the shape of a scattering obstacle using the spectral data of the far field operator." *Inverse problems* **14**(6), 1489-1512 (1998).

[8] Kress, R. "Integral Equation Methods in Inverse Acoustic and Electromagnetic Scattering." in *Boundary Integral Formulations for Inverse Analysis*, D. B. Ingham and L. C. Wrobel eds. Computational Mechanics Publications, South Hampton, UK (1997).

[9] Potthast, R.: "A fast new method to solve inverse scattering problems." Inverse Problems 12, 731-742 (1996).

[10] Potthast, R.: "A point-source method method for inverse acoustic and electromagnetic obstacle scattering problems." IMA Jour. Appl. Math. 61, 119-140 (1998).

[11] Potthast, R.: *Point sources and multipoles in inverse scattering theory.* Chapman & Hall (2001).
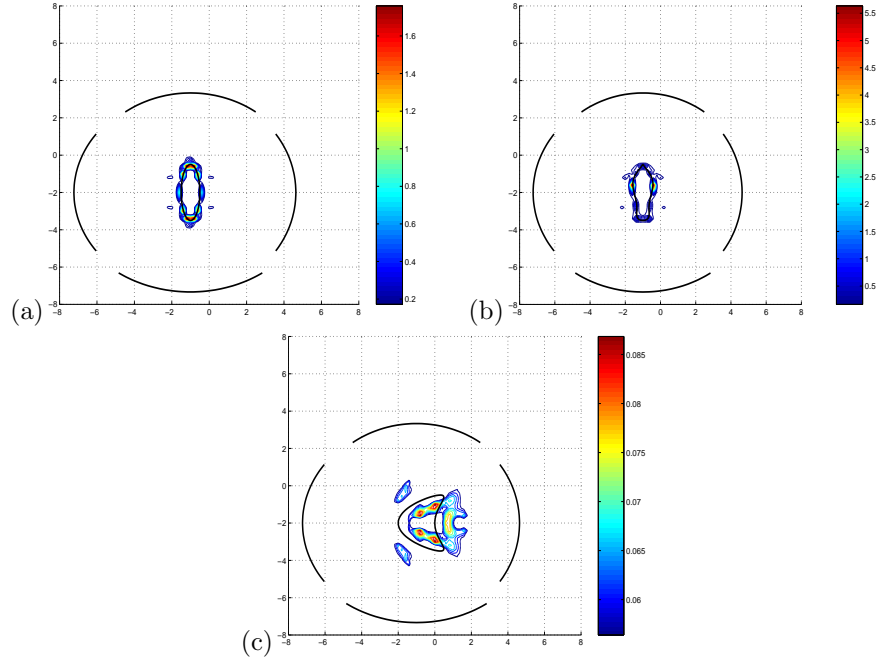
FIG. 4.8. *The* unfiltered, $\mathcal{M}_l = \mathcal{I}$ *for all l, average intensity of the far field reconstructed from the far field data sampled at four different directions corresponding to four different incident field directions. Frames (a)-(c) are the reconstructions of the ellipse, the boat and the kite-shaped objects $(\Omega_1 - \Omega_3)$ respectively. The parameters for all images are wave numbers $\kappa = .75, 1.0833, 1.4167, 1.75, 2.0833, 2.4167, 2.75, 3.0833, 3.4167, 3.75$; aperture opening $\theta = 0.4 * \pi$; views $v = (1, 0), (0, 1), (-1, 0), (0, -1)$; regularization $\alpha = 10^{-12}$.*
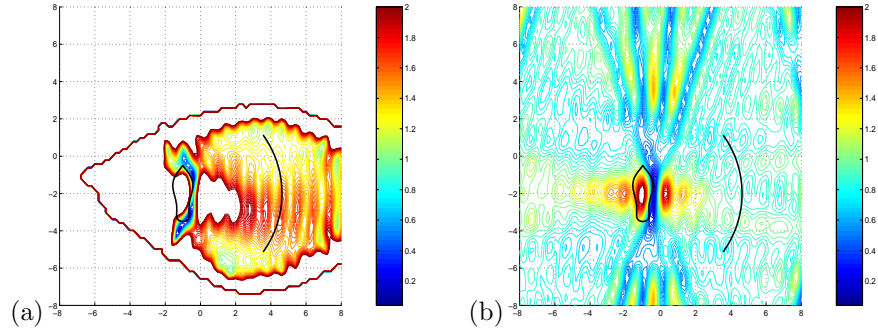

FIG. 4.9. *(a)-(b) the averaged total field intensity calculated via Eq.(3.18) with no filter for obstacle Ω_2 reconstructed from 15 and 3 far field samples respectively. The aperture for each image is held constant at 0.4π independent of the sampling rate. The parameters for all images are wave numbers $\kappa = .75, 1.0833, 1.4167, 1.75, 2.0833, 2.4167, 2.75, 3.0833, 3.4167, 3.75$; aperture opening $\theta = 0.4\pi$; view $v = (1, 0)$; (a) regularization $\alpha = 10^{-5}$, (b) $\alpha = 5x10^{-1}$.*
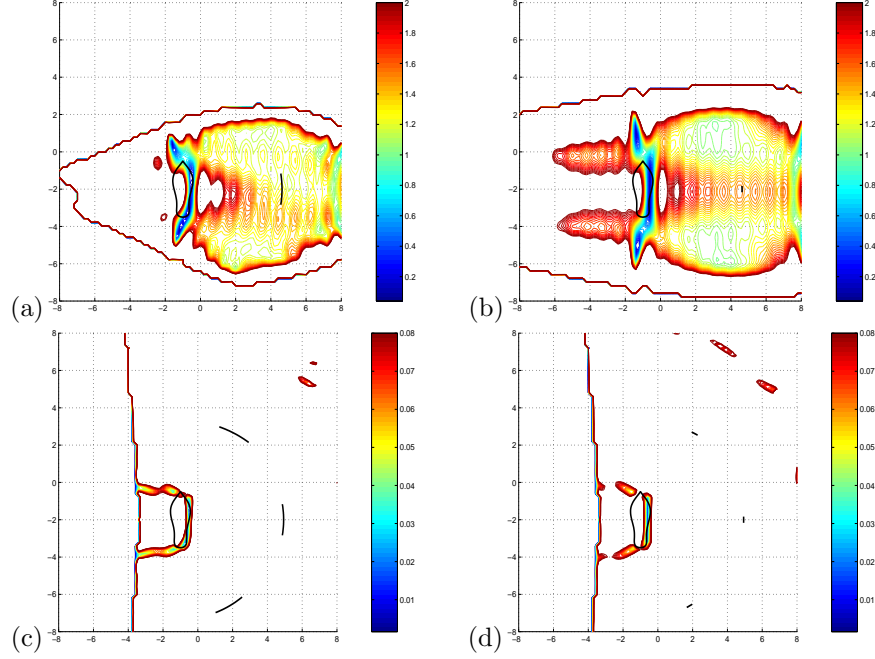
Fig. 4.10. *(a)-(b) a single unfiltered view of the averaged total field intensity calculated via Eq.(3.18) for obstacle Ω_2 with ever smaller apertures. (c)-(d) the averaged total field intensity calculated via Eq.(3.18) with the cone mask given by Eq.(4.4) for obstacle Ω_2 with increasingly smaller apertures. The number of far field samples for each image is held constant at 10 samples independent of the size of the aperture. The parameters for all images are wave numbers $\kappa = .75, 1.0833, 1.4167, 1.75, 2.0833, 2.4167, 2.75, 3.0833, 3.4167, 3.75$; (a), (c) aperture opening $\theta = 0.1\pi$; (b), (d) $\theta = 0.02\pi$; views (a)-(b) $v = (1,0)$; (c)-(d) $v = (1/2, \sqrt{3}/2), (1,0), (1/2, -\sqrt{3}/2)$; regularization (a)-(d) $\alpha = 10^{-12}$.*
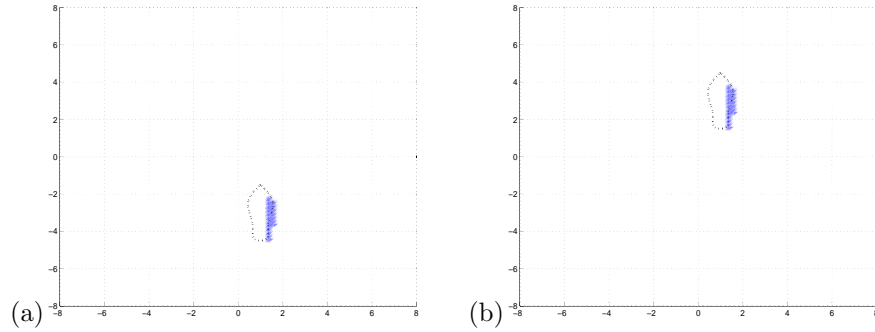

Fig. 4.11. *(a)-(b) show reconstructions by logical image processing with the application of the operators $\mathcal{T}_0$ to $\mathcal{T}_4$ for very small aperture 0.0006π, 10 far field measurements and three different wave numbers. The parameters for all images are wave numbers $\kappa = 1.6, 1.8, 2.0$; aperture opening $\theta = 0.0006\pi$; view $v = (1,0)$; regularization $\alpha = 10^{-12}$.*